Published in final edited form as:
Semin Roentgenol. 2016 October ; 51(4): 317–333. doi:10.1053/j.ro.2016.05.016.

Magnetic Resonanance Imaging of the Liver (Including Biliary Contrast Agents)—Part 2: Protocols for Liver Magnetic Resonanance Imaging and Characterization of Common Focal Liver Lesions

Andrea Agostini, MD[*,†], **Moritz F. Kircher, MD, PhD**[*], **Richard K.G. Do, MD, PhD**[*], **Alessandra Borgheresi, MD**[*,‡], **Serena Monti, MSc**[§], **Andrea Giovagnoni, MD**[†], and **Lorenzo Mannelli, MD, PhD**[*]

[*]Department of Radiology, Memorial Sloan-Kettering Cancer Center, New York, NY.

[†]Department of Radiology, School of Radiology, Università Politecnica delle Marche, Ancona, Italy.

[‡]Department of Radiology, School of Radiology, Università degli Studi di Firenze, Firenze, Italy.

[§]IRCCS SDN, Napoli, Italy.

Introduction

Magnetic resonance imaging (MRI) is a fundamental tool for the noninvasive evaluation of liver pathologies. The anatomical position, the mobility with respiration, and the peculiar hemodynamics of the liver present several issues that have taken advantage from technological advances in MRI technology in the last decade, in particular regarding hardware, software, and contrast media (CM). We provided an overview of these topics in the first part of the review.

MRI pulse sequences of clinical use in liver imaging can be divided into (1) T2-weighted sequences, for detection and characterization of focal and diffuse lesions without contrast, (2) T1-weighted sequences, with or without contrast injection, for further lesion characterization, and (3) additional techniques, such as diffusion-weighted imaging (DWI) and magnetic resonance cholangiopancreatography (MRCP). Most sequences have different names and abbreviations, and the reader is invited to find the respective commercial name specific for each vendor in appropriate references.[1]

The use of CM adds information on function and vascularity of liver parenchyma and focal lesions. The optimization of the technique for postcontrast studies and the basic concepts for characterization of focal liver lesions are briefly discussed in the following sections.

MRI provides several advanced techniques for quantitative evaluation of diffuse liver disease. The complexity of these techniques is beyond the scope of this review, and only a

---

Address reprint requests to Lorenzo Mannelli, MD, PhD, Department of Radiology, Memorial Sloan-Kettering Cancer Center, 1275 York Ave, New York, NY 10065. mannelll@mskcc.org.

brief description on magnetic resonance elastography (MRE), fat and iron quantification would be provided.

At the end of our overview, we would discuss strategies to build basic liver protocols.

Liver MRI Protocol

Patient Positioning

The phased-array coil is positioned at the center of the table. The patient is positioned supine (head or feet first) with the center of the coil aligned with the xiphoid process. After observation of normal patient respiration, the respiratory bellow should be placed at the site with the widest respiratory motion. Special pads are placed cranially and caudally to the bellow to avoid its abnormal compression by the coil. The center of the coil is landmarked with the laser pointers. When necessary (3T scanners), the radiofrequency (RF) pad to reduce B1 inhomogeneities is placed between the anterior abdominal wall of the patient and the receiving coil (*see also the first part of this review*). The variability of the anteroposterior abdominal diameter requires appropriate adjustments of the signal amplification in the middle third of the body to avoid noise breakthrough.[2]

Localizer

Usually rapid sequences providing T2-weighted images are useful: single-shot fast spin echo (SSFSE) and balanced steady state free precession (BSSFP) sequences can acquire the entire volume of the upper abdomen in nearly 20 seconds, with less than 0.5 s/image.[3]

The localizer provides an accurate localization of the patient in the scanner, confirms the inclusion of the interested volume (upper abdomen), and assists the planning of the following sequences. Even if the MRI examination is focused on the liver, most series include other organs and retroperitoneal structures situated in the upper abdomen.

The localizer consists of few images of the upper abdomen with medium-large rectangular field of view, oriented in the 3 planes of the space (axial, coronal, and sagittal). The choice of a low number of thick slices, for example, 3 slices per plane, 10 mm thickness, and high gap to cover the entire field of view of the upper abdomen may be preferred to minimize the acquisition time (Fig. 1). However, some authors prefer a more detailed anatomical coverage by acquiring thinner slices with small interslice gaps to detect eventual collateral or incidental findings (Fig. 1).[4]

T2-Weighted Images

The liver has a relatively low signal on T2-weighted images, whereas most of the hepatic lesions have higher signal than background liver parenchyma owing to their higher fluid content (eg, cysts and hemangiomas) or an imbalance in free and bound water or inflammation or edema in solid lesions.[5]

The spin echo technique represents the standard for T2 imaging of the liver, commonly based on fast spin echo (FSE) and SSFSE sequences. The different design of the sequences has influence on image quality and tissue contrast, thus FSE and SSFSE should be considered complementary more than alternative.

Fast Spin Echo—The FSE sequence is characterized by a 90° excitation pulse followed by multiple 180° refocusing pulses to fill several lines of the k-space (echo train [ET]) within a repetition time (TR). Since the early applications, FSE sequence is preferred over SSFSE because of the higher liver signal-to-noise ratio (SNR) and lesion-to-liver contrast-to-noise ratio (CNR).[6,7] In fast recovery FSE (FRFSE), 2 RF pulses at the end of the (ET) (flip angles: +180° and −90°) restore the magnetization of tissues with long relaxation times before the subsequent excitation pulse, resulting in improved SNR, CNR, and lesion conspicuity.[8,9]

FSE are usually acquired with respiratory triggering or gating, navigators, or breath held. Some authors demonstrated better lesion detection with triggered or navigated FSE sequences, whereas other authors found a better image quality in breath-hold acquisitions with comparable lesion conspicuity. [10,11]

Single-Shot Fast Spin Echo—The SSFSE sequence is characterized by a 90° excitation pulse, followed by multiple 180° refocusing pulses to fill slightly more than half of the k-space; the rest of k-space is reconstructed by using mathematical properties of the Fourier transform. SSFSE has a rapid acquisition time (< 1 s/slice) and can be acquired breath-held. In comparison with FSE and FRFSE sequences, the longer ET of SSFSE may result in lower SNR and CNR and decreased conspicuity of solid lesions due to magnetization transfer effects and blurring artifacts along the phase encoding direction.[7,8,11] The design o this sequence is suitable for acquisition with long echo time (TE) and heavy T2-weighting.[4]

SSFSE and FSE: Artifacts—Image blurring can be reduced by shortening the ET or implementation of parallel imaging.[4]

SSFSE and FSE are both prone to flow artifacts that can affect the evaluation of small liver lesions close to vessels.[12] Moreover, moving fluids in large collections, ascites, or pleural effusions cause proton dephasing resulting in signal loss in the SSFSE sequence (Fig. 2).[4]

NonCartesian k-space filling (Periodically Rotated Overlapping ParallEL Lines with Enhanced Reconstruction) and tridimensional (3D) acquisitions are useful to reduce motion artifacts due to respiration. Moreover, fat has high signal because of the effect of the ET onj-coupling. Fat suppression may be helpful to solve this artifact.[12]

Implementation—T2-weighting provides additional information for lesion differentiation between fluid, benign lesions with long TE (TE > 120 milliseconds, cysts and hemangiomas), and solid or malignant lesions having shorter TE (TE < 120 milliseconds).[13,14] FSE has higher SNR and CNR and is suitable for detection and characterization of solid lesions using TE < 120 milliseconds, whereas SSFSE can be easily adjusted for heavily T2-weighted images (TE > 120 milliseconds).[4]

Fat suppression improves SNR and CNR in liver imaging and is helpful to reduce motion artifacts. [10,12] Several techniques are available to obtain fat suppression, and spectral saturation is usually implemented on high field magnets without B_0 inhomogeneity.[4,15] The longer ET of SSFSE leads to higher signal loss, thus the FSE sequence may be more suitable for fat suppression.[4]

Parallel imaging allows for the reduction of ET length resulting in improving image blurring and lowering energy deposition, in particular, at 3T. NonCartesian filling of the k-space reduces motion artifacts.[4,12,16]

In the basic liver protocol, FRFSE or FSE can be used to acquire moderately T2-weighted axial images (TE < 120 milliseconds) with and without fat suppression, whereas SSFSE sequence provides an overview of the upper abdomen on the axial and coronal plane (Fig. 2).[4]

Additional Sequences: STIR, SPAIR, and BSSFP—Short-tau inversion recovery (STIR) and spectral attenuated inversion recovery (SPAIR) sequences provide T2-weighted images with fat suppression. In STIR, a −180° preparation pulse inverts the longitudinal magnetization, whereas the excitation pulse starts when the longitudinal magnetization of fat is null. In the SPAIR technique, the inversion pulse is spectrally selective for fat, with higher CNR than STIR.[17] The STIR sequence has lower SNR and CNR than FSE and is not the first choice in liver imaging, but it is useful to obtain fat suppression in case of B_0 inhomogeneity and if spectral techniques are not effective.[4,12,17]

BSSFP is not subject to motion artifacts and can be useful in patients with reduced apnea time for the depiction of vascular and biliary anatomy. However, its mixed T1 and T2 signal intensity characteristics make this kind of imaging less useful for lesion detection and characterization.[3,18]

T1-Weighted Images

Precontrast, T1-Weighted Images—Gradient echo (GRE) techniques are the standard for T1-weighted liver imaging.[4,19,20]

Conventional GRE sequences are rarely used because of long acquisition times. Steady state free precession sequences have instead short acquisition time because of a short TR (TR < T2) where a “steady state” is achieved for the longitudinal and transverse magnetizations (eg, spoiled GRE [SPGR]); T1-weighted images are obtained with spoiler gradients and phase shift of RF pulses.[21] Even if the acquisition time is short (the entire liver is covered in ≤25 seconds in one breath-hold), the limitation of 2D SPGR is represented by low sensitivity for small liver lesions: 2D acquisitions require relatively thick slices (≥5 mm), with volume averaging reducing lesion conspicuity and interslice gaps that may lead to incomplete anatomical coverage. Solutions to improve SNR with complete anatomical coverage are represented by multislice acquisitions or 3D sequences.[22,23] In less than 30 seconds, 3D SPGR with undersampling and interpolation of k-space allows acquiring images of the entire liver volume with nearly isotropic voxels. This approach provides thin interleaved slices (4–6 mm interleaved by 2–3 mm), multiplanar reconstructions are also possible, and the sensitivity for small lesions is higher.[19,24] Parallel imaging and nonCartesian filling of k-space acquisition further improve image quality and shorten the image acquisition time.[4,25]

GRE sequences are prone to susceptibility and chemical shift artifacts that can be used to detect and quantify iron and fat deposition within liver parenchyma or focal liver lesions.[26] Chemical shift artifacts are caused by the lower precession frequency of fat protons in comparison to water. These differences lead to periodic phase coherence or opposition of water and fat signals. In-phase coherence (in-phase), the signal from each voxel is the constructive sum of water and fat signal, whereas in phase opposition (out-of-phase) the 2 signals have a phase difference of 180°, and thus the signals null each other out. GRE sequences acquire out-of-phase and in-phase images by recording 2 echoes at specific times within the same TR, usually 2.2 milliseconds and 4.4 milliseconds at 1.5 T, and 1.1 milliseconds and 2.2 milliseconds at 3T for out-of-phase and in-phase images, respectively. In case of liver steatosis (or some fat-containing lesions), a significant amount of fat is present in the cytoplasmic compartment and within the same voxel: in-phase images would show the added signal of water and fat, whereas out-of-phase images show hypointensity because of signal cancellation.[15]

Iron deposition causes susceptibility artifacts because of the T2* effect: the rapid signal decay is detectable as hypointensity at longer TEs.[27]

In clinical practice, independently of the B_0 field strength, it is important to set the GRE T1-weighted sequence with TEs as short as possible, with the out-of-phase dataset acquired with a shorter TE than the in-phase dataset, to avoid misleading findings in case of associated iron overload and liver steatosis.[4]

Dixon techniques use algorithms that process in-phase and out-of-phase to separate and quantify water and fat signal. With these algorithms, it is possible to obtain in-phase and out-of-phase images, as well as fat suppression. This technique can be used for fat fraction quantification.[15,25]

T1-Weighted Imaging: Contrast-Enhanced Study—Postcontrast phases are performed with fat suppressed 3D SPGR, with 20–30 seconds breath-hold acquisitions covering the entire liver volume. Fat suppression can be achieved with different techniques, depending on the available scanners.[12,15,19]

After paramagnetic CM injection, subsequent acquisitions at specific time points highlight perfusion differences between the liver parenchyma (20%-30% sustained by the hepatic artery and 70%-80% by the portal vein) and focal lesions, and among different focal lesions. The bulk of the contrast administered is delivered to the liver by the portal vein, whereas hepatic lesions, in particular the malignant ones, are usually perfused by neovascularization through branches of the hepatic artery.[28] Hepatospecific CM provide additional functional information to vascular findings. The following precontrast and postcon-trast phases are acquired (Fig. 3).

1. *Baseline (precontrast) acquisition*. It ensures adequate technical quality and anatomical coverage of the liver. It also represents the reference to evaluate enhancement characteristics of focal lesions and liver parenchyma. Some hepatic lesions are hyperintense on T1-weighted images, and subtraction techniques help evaluate the presence of

enhancement of these lesions. For this reason, technical uniformity in acquisition of all the precontrast and postcontrast phases is required.[4,12]

2. *Arterial phase*. This phase is important to detect and characterize hepatic lesions with arterial vascularization, which can be benign (eg, focal nodular hyper-plasia [FNH]) or malignant (eg, hepatocellular carcinomas [HCC] and some types of metastasis), as well as treatment response of HCC. Liver imaging reporting and data system criteria define the arterial phase by a fully enhanced hepatic artery, without enhancement by anterograde flow of hepatic veins. This phase can be further divided into early and late arterial phase. In the early arterial phase, there is no enhancement of the portal vein. This early arterial phase is ideal for the evaluation of the arterial anatomy but is inadequate for detection of arterially enhancing lesions. The late arterial phase presents enhancement of portal branches and is required for the further evaluation of arterially enhancing lesions (Fig. 3).[29] Accurate timing is necessary as the time window of the first arterial passage of most CM is narrow and short than the acquisition time of 3D SPGR sequences. To achieve the desired contrast, the passage of CM in the arterial liver district has to occur when the central portion of k-space is sampled.[30] Several methods are available to achieve this result:

   a. *Fixed delay*. It consists of starting the image acquisition with a fixed delay between CM injection and tumor enhancement, estimated to be 32.4 ± 5.9 seconds in healthy subjects.[31] Unfortunately, the time between injection and arterial enhancement is dependent on cardiac function and other factors, and fixed delay achieves a correct arterial enhancement in merely 61% of cases.[32] This technique is recommended only if tracking techniques are not available on the scanner.

   b. *Test bolus*. A single axial SPGR slice of the upper abdomen (eg, through the celiac axis) is repeatedly acquired with short intervals (1–2 seconds) after the administration of a small bolus of CM (eg, 1–2 mL), followed by a saline flush (15–30 mL), using a power injector. A software plots aortic signal toward time, generates a curve, and demonstrates a peak as the test bolus passes through the aorta. The timing of the late arterial phase is calculated based on the time from the bolus injection to the aortic peak ($\text{Time}_{\text{aorta}}$) and a fixed delay ($\text{Time}_{\text{aorta-liver}}$) of 4–10 seconds from the aortic peak to the arterial liver enhancement.[30,31] Further, 3 additional parameters are necessary to calculate the delay between the contrast injection and the image acquisition for the late arterial phase: the time needed for the injection of the entire amount of contrast (Time_{Inj}), the time needed for the image acquisition (Time_{seq}), and the time of sampling of the central portion of k-space within the pulse sequence. For example, if the central portion of the k-space is acquired at half time of the sequence, then the acquisition delay from the time of starting the injection is $1/2\ \text{Time}_{\text{Inj}} + \text{Time}_{\text{aorta}} + \text{Time}_{\text{aorta-liver}} + 1/2\ \text{Time}_{\text{seq}}$. This technique may be easy to implement but requires extra CM to be administered.

   c. *Bolus Tracking*. The technique consists in sampling a tracker volume (eg, at the level of the celiac axis) with a high temporal resolution. The arterial phase is automatically started when the aortic signal surpasses a threshold, with a fixed delay from the aortic peak to arterial liver enhancement (4–10 seconds).[31,33] This technique does not need additional administration of CM, but requires better collaboration from the patient because of the noise produced by the bolus tracking sequence (Tables 1–3).

3. *Portal venous phase*. In this postcontrast phase, the portal vein branches and the hepatic veins are fully enhanced. The liver parenchyma is at the enhancing peak; this phase is essential for lesion detection and characterization.[29] In particular, malignant lesions have arterial vascularization (neovascularization) and none or minimal portal inflow, in general presenting a lower signal than the liver parenchyma nearby (Fig. 3).[28] The portal venous phase is reached at an average estimated time of 54.2 ± 10.8 seconds from the contrast injection; however, in cirrhotic livers owing to perfusion changes, this phase tends to be delayed (Tables 1–3).[31]

4. *Delayed phase*. The delayed phase is characterized by the enhancement of the portal branches, the liver parenchyma, and the hepatic veins; in this phase the enhancement is less intense and more uniform in comparison to the portal venous phase, thanks to the contrast circulation and distribution in the vascular and extravascular compartments. It should be acquired between 3 and 5 minutes from bolus injection.[29] The clinical utility of the delayed phase is the depiction of the washout of hyperenhancing lesions (eg, HCC) or the late enhancement or “pooling effect” of stromal components of some lesions (hemangiomas, scar in FNH or desmoplastic reaction of cholangiocarcinoma, and cholangiocellular carcinoma [CCC]) after the administration of an extracellular or interstitial CM.[28,29,34,35] The peculiar pharmacokinetics o Gd-EOB-DTPA (Gadoxetate, Primovist/ Eovist, Bayer, Germany), and in particular the rapid liver uptake, does not allow the acquisition of a delayed phase, in this case liver imaging reporting and data system guidelines recommend to call this a "transitional phase" (Fig. 3 and Tables 1–3).[29]

5. *Hepatospecific phase*. This phase is characterized by hyperintensity of hepatic parenchyma in comparison to intrahepatic vessels and by the presence of biliary excretion of CM. The different kinetics of hepatospecific CM result in different timing of the hepatospecific phase, usually 15–20 minutes for Gd-EOB-DTPA and 60–90 minutes for Gd-BOPTA (Gadobenate dimeglumine, Multihance, Bracco, Italy) since CM injection.[36] These times may be longer in cirrhotic livers (Fig. 3B and C; Table 2)[4,29,37].

Enhancement Curves of Extracellular or Interstitial CM, Gd-BOPTA, Gd-EOB-DTPA, and the Role of MS-325—The differences in enhancement curves of hepatic parenchyma, vessels, and lesions with Gd-EOB-DTPA, Gd-BOPTA, and extracellular or interstitial CM have been explained with quantitative signal analysis and perfusion studies. The differences in imaging protocols, signal analysis (SNR, CNR, or signal intensity), and contrast doses provided results that were at times discordant.[36]

Gd-EOB-DTPA has a considerable hepatocellular uptake (~50%), starting in the early portal venous phase (~40 seconds since the injection), whereas hepatocellular uptake of Gd-BOPTA is slower and involves a smaller fraction (approximately 5%) of the administered dose, thus Gd-BOPTA distribution within the first 5 minutes is similar to extracellular or interstitial CM (Fig. 3).[39,45–47]

The signal of liver parenchyma after extracellular or interstitial CM injection increases to a peak during the portal venous phase and then decreases progressively in the following minutes (Fig. 3A).[42] After Gd-EOB-DTPA injection, the signal of the liver parenchyma keeps increasing from the portal phase for another 20 minutes as it reaches a plateau that is lasting for approximately 20 minutes. Liver signal starts decreasing at 40 minutes after injection (Fig. 3B).[36,39,42] After Gd-BOPTA injection, the peak of liver enhancement and SNR is during the portal phase, with a subsequent slow increase of liver parenchyma signal, reaching a plateau at 60 minutes and lasting for approximately 60 minutes, when liver enhancement starts to decrease. Thus, for Gd-BOPTA the optimal timing of the hepatospecific phase is within 60 minutes and 120 minutes (Fig. 3C).[36,40–44]

In vascular phases during the first 5 minutes, Gd-EOB-DTPA achieves lower signal than Gd-BOPTA and extracellular or interstitial CM within abdominal aorta, portal vein, and hepatic veins.[36,38–41] The rapid clearance of Gd-EOB-DTPA from the vascular compartment results in marked hypointensity of intrahepatic vessels in the hepatospecific phase (Figs.3B, 4F, and 5C). MS-325 (Gadofosveset troisodium, Ablavar, Lantheus Medical Imaging, USA) may be useful in hepatic studies if administered after the dynamic study with Gd-EOB-DTPA for a better detection of small hypointense lesions close to hepatic vessels.[48]

Optimization of Technique—When performing postcontrast studies with fat suppressed, breath-hold 3D SPGR, the suggested slice thicknesses are 4–6 mm with an inter leave of 2–3 mm.[4,19,23] Dixon techniques provide the best quality of fat suppression.[4,25]

The optimization of scanning delays after CM injection requires an automated injector, possibly with double syringe, delivering a bolus of CM (usually at a rate of 2–3 mL/s) followed by a saline flush (20–30 mL).[30–33]

Injection of Gd-EOB-DTPA presents some technical problems. The lower approved dose results in a small injected bolus leading to truncation artifacts. A possible solution is a slow injection rate (of 1 mL/s).[37,49] Moreover, Gd-EOB-DTPA causes transient dyspnea in 14% of patients resulting in motion artifacts on the arterial phase.[50] These problems can be reduced by using motion-resistant techniques, such as fast image acquisition sequences for the acquisition of multiple arterial phases.[50,51]

Flip angle in SPGR is chosen to optimize image SNR and partially image contrast.[48,52]

Considerations for Characterization of Liver Lesions—A complete review of the differential diagnosis of focal liver lesions is beyond the scope of this review. In this paragraph, we would discuss the basic imaging findings of common focal liver lesions with regard to contrast materials.

Liver hemangioma (LH) is the most common focal lesion, with a prevalence of 20% in the general population.[34] Typical imaging findings on MRI are the high signal on T2-weighted images and hypointensity on T1-weighted images; imaging features can be more complex in case of large, giant, and sclerosed hemangiomas. After extracellular or interstitial CM or Gd-BOPTA, LHs have 3 possible enhancing patterns depending on lesion size: (1) small lesions with rapid filling, (2) medium lesions with peripheral nodular enhancement and centripetal filling, and (3) large lesions with geographic enhancement, with isointensity to vascular branches in the late venous phases; these large (giant) hemangiomas require longer time for complete filling.[53] Although Gd-BOPTA has a distribution similar to extracellular or interstitial CM during the first 5 minutes, the rapid hepatocellular uptake of Gd-EOB-DTPA leads to impaired pooling of CM within LHs: this causes “pseudo-washout” effect with almost incomplete filling and hypointensity in the transitional phase.[54] The differential diagnosis with malignant lesions is more difficult, and inconclusive findings may occur in up to 20% of patients.[53] Because of this reason, at our institution, we prefer to obtain the baseline MRI using extracellular or interstitial CM or Gd-BOPTA.

FNH has a prevalence of 3%-8% in the general population, higher in women than in men.[34] It is a benign lesion composed by normal hepatocytes forming multinodular structures around a central scar. Typical findings on MRI are isointensity-hypointensity on T1-weighted images and isointensity-hyperintensity on T2-weighted images; the central scar is present in only 20%-30% of cases.[55] FNH has an arterial supply with strong arterial enhancement and subsequent isointensity or slight hyperintensity to liver parenchyma in the late vascular phases. When present, the central scar demonstrates a late enhancement after the administration of extracellular or interstitial CM and Gd-BOPTA.[34,56] Imaging findings during vascular phases are quite typical but overlap with other lesions, in particular with hepatocellular adenoma (HA) or malignant lesions. In the hepatospecific phase after both Gd-EOB-DTPA and Gd-BOPTA, FNH are isointense or slightly hyperintense to liver parenchyma because of prolonged hepatocellular CM uptake (Fig. 4). The isointensity-hyperintensity in the hepatospecific phase can be explained by the presence of deranged biliary ducts within the lesion, and have high accuracy in discriminating FNH from HA or malignant liver lesions.[55–57]

HA is less common than FNH, and it is associated with several medical conditions such as glycogen storage disease (glycogenosis type 1), diabetes (mature-onset diabetes of the young, MODY3), and the use of oral contraceptives (Fig. 5). Larger lesions (>5 cm) are at risk of bleeding and malignant transformation: for these reasons, accurate diagnosis is necessary and surgical management is often recommended.[55,58] Recently, HAs have been divided into 4 subtypes by genetic and molecular profiles: inactivation of HNF1α, activation of β-catenin, inflammatory subtype, and unclassified.[58] Imaging findings on T1- and T2-weighted images are variable due to possible presence of intralesional fat, hemorrhage, or glycogen. Some imaging characteristics correlate with molecular features (eg, fat content and mutation of HNF1α).[34,58] Postcontrast findings are characterized by arterial enhancement, which however is nonspecific as it overlaps with other liver lesions, in particular with FNH and some malignant lesions. The absence of biliary ducts and the lower expression of membrane transporters than FNH results in lack of uptake of hepatospecific CM and thus hypointensity in the hepatospecific phase: this finding has high accuracy in the differential diagnosis with FNH (Figs. 4 and 5); accuracy in differentiation between HA and other solid, nonuptaking liver lesions can be lower.[56,59]

Liver is a common site of metastases, which represent the most common hepatic malignant lesions. As metastases do not contain functioning hepatocytes, they do not demonstrate prolonged uptake of hepatospecific CM.[56] Hepatospecific CM in comparison with extracellular or interstitial CM improve detection and characterization of liver metastases, with important consequences on clinical management (Fig. 6).[60,61]

HCC is the most common primary liver malignancy, with liver cirrhosis as the most important risk factor. Hepatocarcino-genesis from regenerative nodules to HCC is well known; the radiological diagnosis of HCC relies on enhancement in the arterial phase with washout in the portal venous or delayed phases (enhancement curves in Fig. 3). The histopathological basis of these findings in HCC is the presence of neovascularization with blood supply through the hepatic artery, and progressive loss of portal vascularization.[62] However, these imaging findings are frequently recorded in advanced HCC, with moderate or low differentiation grade. Early HCC or high-grade dysplastic nodules may not have enough neovascularization and present with atypical enhancement pattern in variable percentages in different case series, usually in 10% of cases, but up to 40%. Using vascular diagnostic criteria, the magnetic resonance diagnosis of these atypical nodules is challenging.[63,64] The loss of cellular differentiation during hepatocarcinogenesis leads to altered expression of membrane transporters. In most HCCs, this results in a reduction of membrane transporters (in particular organic anion-transporting polypeptide) with reduced hepatocellular uptake of hepatospecific CM and hypointensity in the hepatospecific phase. A minor portion of HCC, however, is associated with hyperexpression of membrane transporters with increased uptake of hepatospecific CM and hyperintensity in the hepatospecific phase.[62,64–66] Signal intensity in the hepatospecific phase is correlated with expression of transporters, and some authors found a correlation between imaging findings in the hepatospecific phase, mutation of β-catenin, and differentiation.[66,67] However, the hypointensity in the hepato-specific phase is a strong indicator of malignancy with high sensitivity, negative predictive value, and accuracy; the functional information provided by hepatospecific CM improves diagnostic sensitivity of up to 15% for the diagnosis of HCC.[64,68]

CCC is the second most common primary hepatic tumor, and an intrahepatic CCC (iCCC) mass represents 10% of all CCC. Imaging findings are not specific: usually it is isointense to hypointense on T1-weighted images and isointense-hyperintense on T2-weighted images, but subject to variations due to mucin, necrosis, and desmoplastic reaction. Usually capsular retraction and vascular infiltration are present. After the administration of extracellular or interstitial CM, an iCCC typically presents with peripheral enhancement proceeding in a centripetal direction toward the desmoplastic component, which shows late enhancement. Small iCCCs, where desmoplastic reaction is less dominant, may demonstrate only arterial enhancement, making it difficult to differentiate them from other hepatic lesions. After the administration of Gd-BOPTA or Gd-EOB-DTPA, the peripheral component becomes hypointense in the hepatospecific phase while the central desmoplastic reaction may retain a small quantity of CM resulting in mild central hyperintensity (Fig. 7).[35,56] Hepatospecific CM can be useful in surgical planning because of the improved conspicuity of satellite nodules in the hepatospecific phase.[35]

Diffusion-Weighted Imaging

DWI is based on the Brownian motion (or diffusion) of water molecules during image acquisition. The detection of movements of water molecules is obtained by applying water motion probing gradients before and after the 180° refocusing pulse, and the diffusion weighting is dependent on the parameter b. The b values to be chosen for liver imaging are not well established. Usually, image datasets using 3 different b values are acquired: (1) $b = 0$ s/mm^2: very similar in appearance to T2-weighted imaging with good anatomical details, (2) $50 < b < 100$ s/mm^2: SNR is still high with imaging appearance similar to T2 but with the advantage of blood flow suppression (black blood), and (3) $400 < b < 800$ s/mm^2: these images have low SNR but high contrast between lesions and background liver parenchyma.[69]

The main application of DWI in liver imaging is as a complementary sequence for lesion detection and characterization. In particular, DWI has demonstrated high sensitivity in the detection of small liver lesions, in particular using low b values due to blood flow suppression and high contrast between lesions and background liver parenchyma.[70,71] DWI can be particularly useful in patients with contraindications to CM. DWI cannot replace postcontrast studies in lesion characterization, because apparent diffusion coefficient (ADC) values overlap between benign and malignant liver lesions, but it increases confidence in lesion characterization when used in combination with other sequences (Figs. 6 and 7).[69,72] Other interesting applications of DWI are in the evaluation of treatment response, where DWI changes are associated with change in cellularity of tumoral lesions.[69] The roles of ADC and intravoxel incoherent motion in chronic liver disease and lesion characterization are still to be defined.[72]

DWI images are usually obtained with a single-shot echo planar imaging spin echo sequence with T2-weighting (TE: 60–100 milliseconds) and fat suppression. Echo planar imaging (EPI) sequences are prone to motion artifacts, susceptibility, and B_1 inhomogeneity. Breath-hold acquisitions have the advantage of reduced blurring and ghosting artifacts, but the short acquisition time limits the number of excitations, spatial resolution, and number of *b* values. Navigator or respiratory-triggered techniques require longer acquisition times but improve image SNR, in particular, at higher *b* values and reduce motion artifacts and blurring.[72] With the use of parallel imaging, it is possible to reduce the ET length, allowing for higher spatial resolution and reduced susceptibility artifacts to be achieved.[73]

DWI should be included in routine liver protocols because it improves sensitivity for lesion detection and increases reader confidence in lesion characterization.[69]

Magnetic Resonance Cholangiopancreatography

MRCP is a noninvasive technique for the study of the biliary tree and pancreatic ducts.

The basic protocol for studying the pancreaticobiliary tree requires heavily T2-weighted sequences. Heavily T2-weighted sequences represent the high water content of the biliary fluid while soft tissues nearby are suppressed. MRCP studies are never performed without acquiring the basic sequences for evaluation of hepatic and pancreatic parenchyma.[4] MRCP evaluates anatomical variants as well as benign and malignant pathologies of the pancreaticobiliary tree.[74]

MRCP images are obtained using SSFSE and FSE sequences. In this setting, both sequences are heavily T2-weighted, while SSFSE can also be used to obtain T2-weighted images.

1. Coronal (and axial) SSFSE, T2-weighted (TE: 70–110 milliseconds). This sequence is routinely implemented in the basic liver protocol to obtain axial and coronal T2-weighted images for a general overview of the upper abdomen. The T2-weighting is set to enhance physiological and pathological fluids without suppression of soft tissues.[75,76]
2. Thick-slab SSFSE, heavily T2-weighted. This technique acquires thick slices (30–80 mm) during a few breath-holds. The acquisition planes are radial and centered on the long axis of the main biliary duct. The acquisition using long TEs (eg, ≥900 milliseconds) gives high signal to fluid components while soft tissues are suppressed because of shorter relaxation times. The main advantages are the short acquisition times without any postprocessing required; the rapid acquisition time is particularly useful in patients unable to hold their breath. The drawback is in the thickness of the slices: detection of biliary stones may be affected by volume averaging artifacts, and close anatomical structures (gastrointestinal content or renal cysts) may project on the biliary tree. The per os administration of superparamagnetic CM, or pineapple juice naturally rich of manganese, would suppress signal from fluid in the bowel.[76]

3. Coronal oblique, 3D FSE, or FRFSE, heavily T2-weighted (TE > 650 milliseconds). These sequences provide thin slides (1–3 mm) interleaved or with no gap, with almost isotropic voxels of ~ 1 mm. The main advantage is in the high spatial resolution in the 3 spatial planes and the possibility of multiplanar and 3-dimensional reconstructions. The drawbacks are the long acquisition times caused by the necessary respiratory triggering or gating (3–5 minutes).[75–77]

Recent hardware and software developments have improved the image quality of MRCP. In particular, parallel imaging allows faster acquisitions and reduces blurring artifacts of SSFSE sequences. The 3-dimensional acquisitions with FSE or FRFSE provide images with better spatial resolution, SNR, and bile duct visualization than 2D sequences. NonCartesian filling of k-space improves image quality, and imaging at 3T benefits in specific absorption rate reduction from variable flip angle refocusing techniques.[78,79]

Advanced Techniques

Diffuse Liver Diseases: Iron and Fat Quantification

Liver steatosis is the basis of nonalcoholic fatty liver disease, the most common chronic liver disease in the western world, and represents a risk factor for liver cirrhosis and HCC. As it is a reversible condition, an accurate estimation of fat overload is important for diagnosis and follow-up.[80]

The reference standard for liver fat quantification is liver biopsy. However, this is invasive and prone to sampling errors. MRI is able to separate fat and water signal because of the different resonance characteristics; chemical shift imaging and Dixon techniques implemented in the basic liver protocol provide an alternative to biopsy for liver fat quantification.[81]

Postprocessing of in-phase and out-of-phase images allows quantifying the liver fat content on a scale from 0%-50%: this may be a technical limitation but still suitable for liver studies.[15,81] The proton density fat fraction uses a more complex model for fat estimation: images are acquired using 2D multiecho GRE to eliminate the confounding factors (T1, T2, T2* bias, spectral complexity of fat, noise, iron, etc.). This technique provides a full range fat fraction (0%-100%).[82,83]

Iron metabolism is strictly regulated in physiological conditions. Iron overload can be caused by increased absorption due to a deregulated metabolism or by repeated transfusions. Liver is one of the storage organs, and iron overload may lead to chronic liver damage and cirrhosis. Liver biopsy is the reference standard for liver iron quantification, but is invasive and prone to sampling error.[80]

MRI is highly sensitive to the presence of iron due to its superparamagnetic properties. The presence of iron can be evaluated qualitatively with T2-weighted (FSE) or T2* (GRE) weighted sequences. Moreover, while performing GRE dual-echo T1-weighted sequences, the T2* effect is evident on image datasets acquired with longer TEs (in general the in-phase series, where this appears as signal loss within the liver parenchyma). [4,26,27]

Several methods are available for liver iron quantification, mostly based on T2 or T2* relaxation or relaxometry (R2 and R2*). The first approach requires acquisition of multiple GRE sequences with different flip angles and TE. During the postprocessing, liver signal intensity is compared with non–iron-storing organs (eg, muscle).[27]

Relaxometry methods acquire images with multiecho techniques (FSE or GRE) to evaluate R2 or R2* from signal decay; R2* and R2 relaxivity values correlate with iron deposition. [84,85]

Design of multiecho FSE for estimation of R2 depends on the expected iron overload: the first TE is as short as possible (≤ 5 milliseconds), and the longest echo is usually set at 15–30 milliseconds. The main advantages of this technique are the lower sensitivity to susceptibility artifacts and the high reproducibility. The drawbacks are the long acquisition time with limited anatomical coverage.[86]

R2* relaxometry is performed with multiecho SPGR (2D or 3D). To optimize the fitting with the mathematical model of signal decay, the first TE should be as short as possible (< 1 milliseconds). Usually the last echo is recorded at 10–15 milliseconds. Signal analysis is performed with exponential models to calculate R2*. The main advantages are the shorter acquisition times (breath-hold acquisition, -~20 seconds) and the higher sensitivity to low iron concentrations, and the availability on 1.5 T and 3 T.[86] GRE T2 -weighted sequence is prone to chemical shift artifact of type 2, because phase coherence and opposition of water and fat induces oscillation on signal decay and the exponential model loses in accuracy; this results in the typical sinusoidal decay of the signal with impaired fitting of measurements to the exponential model and lower accuracy in R2* estimation (Fig. 8). A partial solution to this problem is setting TEs when water and fat signal are in phase coherence. Another solution is the application of fat-suppression techniques (eg, STIR techniques with loss in SNR) or fat-corrected R2* estimation.[27,87]

Relaxometry methods with R2 and R2* techniques can be considered accurate in comparison with liver biopsy within a range of iron concentrations owing to technical reasons. In particular, the nonlinear relation between R2 and iron concentration on biopsy specimen, as well as the design of the sequence, may affect the estimation at extreme values; the linear relationship between R2* and iron concentration at biopsy allows a good accuracy of estimation of low iron concentrations whereas estimation of higher iron concentrations is limited because the exponential T2* decay requires very short TEs.[27,86] This is not a relevant problem in the management of these patients. In fact, in case of mild iron overload and low liver concentrations, there are concerns about toxicity of chelating therapy; the lower accuracy in estimation of higher iron concentrations in the different grades of severe overload does not change significantly the therapeutic strategy, whereas the high accuracy of MRI estimations within the intermediate range of iron concentrations provides the indication to the chelating treatment.[85]

Magnetic Resonance Elastography

Liver fibrosis is a consequence of several chronic injuries, further leading to cirrhosis and HCC. Accurate staging of liver fibrosis is clinically relevant because it correlates with morbidity and mortality and also because early stages of fibrosis are reversible.[88] Liver biopsy is the reference standard in the evaluation of hepatic fibrosis, but has several limitations such as the small sampled volume and the invasiveness; several histopathological scores have been developed (eg, METAVIR, Ishak).[89,90]

MRE is a noninvasive alternative to biopsy. The basic idea of MRE is that fibrotic liver has different mechanical properties from the normal liver, resulting in different propagation of mechanical waves. MRE is performed applying a mechanical (in general pneumatic) transducer to the right upper abdominal quadrant. This generates mechanical shear waves (50–60 Hz) propagating through the liver parenchyma. The proton displacement induced by these shear waves is detected using GRE or EPI sequences with motion-encoding gradients. Further processing involves inversion algorithms to calculate stiffness maps and thus quantitatively estimate mechanical properties of liver parenchyma.[91,92] This technique is accurate in staging liver fibrosis, in particular the advanced stages.[93]

Another promising application of MRE is in the characterization of focal liver lesions; however, the experience in this field is still limited and it is not routinely implemented.[94]

Optimization of Liver Protocol

To optimize the liver magnetic resonance protocol, some aspects have to be considered. For example, patient comfort ensures better collaboration. This is important for both image quality and magnet time optimization.

At our institution, a coronal T2-weighted SSFSE sequence is acquired to obtain an overview of the upper abdomen at the beginning of most MRI studies. Axial T2-weighted FRFSE and axial EPI DWI are acquired before the administration of CM. Both FRFSE and SSFSE are moderately T2-weighted (<120 milliseconds). We use spectral fat suppression in FRFSE. The dynamic contrast study is performed using bolus tracking: the arterial phase starts 5 seconds after the aortic enhancing peak; the portal venous phase is acquired 60 seconds after the aortic enhancing peak, and the late venous phase at 3 minutes after the aortic enhancing peak (Table 1).

The postcontrast study has a central role in lesion detection and characterization, and it should be acquired as soon as possible, in particular when using Gd-EOB-DTPA.[12] After acquisition of vascular phases with Gd-EOB-DTPA, there is a lag-time of nearly 15 minutes before the hepatospecific phase is acquired, which represents a time window during which other sequences can be acquired. Naturally, only sequences not negatively affected by the presence of gadolinium should be acquired after contrast injection.[4]

The effects of CM on T2-weighted sequences depend on the type of sequence, lesion to be characterized (solid or nonsolid), and CM distribution and concentration within hepatocytes (in particular considering the rapid uptake kinetics of Gd-EOB-DTPA). In general, SSFSE is more sensitive to T2-shortening by paramagnetic CM, but quantitative signal analysis provided results similar to FSE.[95] Some authors found a decrease in liver SNR with gain in lesion-to-liver CNR when studying solid liver lesions with FSE and STIR sequences after

Gd-EOB-DTPA.[96] These effects on tissue signal can vary depending on CM concentration and the image acquisition time (more or less than ~ 10 minutes since injection).[96,97]

Postcontrast

T2-weighted SSFSE image acquisition should be performed as soon as possible, as high concentration of Gd in the renal pelvis and the biliary tree may affect the evaluation of these areas.[51] Gd-EOB-DTPA has an influence on DWI, in particular the signal intensity and ADC values of liver parenchyma are lowered in the presence of CM. However, signal intensity, CNR, and ADC values of liver lesions do not change significantly, with minor effects on lesion detection.[97–99] In our institution, when Gd-EOB-DTPA is used, all T2-weighted and DWI images are acquired after contrast injection. Because of the high incidence of postinjection transient dyspnea (14% of patients) and truncation artifacts associated with the use of Gd-EOB-DTPA, a slow injection rate and acquisition of multiple arterial phases with techniques oversampling the central portion of the k-space is preferred (Table 2).[50]

MRCP studies can be performed with or without CM injection, and Gd-EOB-DTPA is rarely used in this setting. In the protocol we implemented in our institution, 3 moderately T2-weighted sequences are acquired before CM injection on axial and coronal planes. In particular, fat suppression is obtained with axial FRFSE, whereas SSFSE is used for axial and coronal planes. DWI is acquired before CM injection, whereas MRCP sequences are performed after CM injection. In this setting, CM present in liver parenchyma and the portion concentrating in the urinary tract can be helpful to lower the signal of renal pelvis and liver parenchyma. Usually 3D FRFSE represents the first choice for MRCP. However, if the respiration is inconsistent and respiratory triggering does not achieve adequate image quality, MRCP with thick radial slab using SSFSE and free-breath can provide better image quality (Table 3).

Regarding iron quantification, at our institution we implemented a protocol based on R2* relaxometry. After acquisition of T2- and T1-weighted sequences, we performed 3 multiecho GRE sequences with TEs set in the following 3 ways: (1) TEs to record water and fat phase coherence; (2) short TEs and ETs to investigate the early signal decay in high iron overload; and (3) long ET and longer TEs to improve sensitivity in case of low iron concentrations (Table 4).

Conclusion

In this article, we reviewed the principal information to build an MRI protocol for the study of the liver. We provided an overview on the pulse sequences mostly used in liver MRI protocol, the postcontrast studies, and the additional techniques such as DWI and MRCP. We also discussed about the basic information on the enhancement curves after the administration of different CM, and we described the image findings, in particular in postcontrast studies, of the common focal liver lesions. Finally, we outlined the advanced techniques, and we illustrated the protocols implemented at our institution.

Liver MRI is a field in continuous expansion, taking benefit of the rapid introduction of technical improvements. A multitude of sequences, software, and hardware solutions are becoming available to optimize and tailor the MRI liver study to the patient. Only the deep knowledge by the radiologist with the technologists' complementary contribution allows for an optimal usage of these technologies maintaining the highest quality standards.

Acknowledgments

MSK Cancer Center Support Grant/Core Grant (P30 CA0087).

References

1. Nitz WR. MR imaging: Acronyms and clinical applications. Eur Radiol. 1999; 9:979–997. [PubMed: 10370004]
2. Elmaoğlu, M.; Çelik, A. MR Physics, Patient Positioning, and Protocols. Springer; 2012. MRI Handbook. http://dx.doi.org/10.1007/978-1-4614-1096-6
3. Herborn CU, Vogt F, Lauenstein TC, et al. MRI of the liver: Can true FISP replace HASTE? J Magn Reson Imaging. 2003; 17:190–196. [PubMed: 12541226]
4. Guglielmo FF, Mitchell DG, Roth CG, et al. Hepatic MR imaging techniques, optimization, and artifacts. Magn Reson Imaging Clin. 2014; 22:263–282.
5. Albiin N. MRI of focal liver lesions. Curr Med Imaging Rev. 2012; 8:107–116. [PubMed: 23049491]
6. Schwartz LH, Seltzer SE, Tempany CM, et al. Prospective comparison of T2-weighted fast spin-echo, with and without fat suppression, and conventional spin-echo pulse sequences in the upper abdomen. Radiology. 1993; 189:411–416. [PubMed: 8210368]
7. Coates GG, Borrello JA, McFarland EG, et al. Hepatic T2-weighted MRI: A prospective comparison of sequences, including breath-hold, half-Fourier turbo spin echo (HASTE). J Magn Reson Imaging. 1998; 8:642–649. [PubMed: 9626880]
8. Augui J, Vignaux O, Argaud C, et al. Liver: T2-weighted MR imaging with breath-hold fast-recovery optimized fast spin-echo compared with breath-hold half-Fourier and non-breath-hold respiratory-triggered fast spin-echo pulse sequences. Radiology. 2002; 223:853–859. [PubMed: 12034959]
9. Akin O, Schwartz LH, Welber A, et al. Evaluation of focal liver lesions: Fast-recovery fast spin echo T2-weighted MR imaging. Clin Imaging. 2006; 30:322–325. [PubMed: 16919552]
10. Huang J, Raman SS, Vuong N, et al. Utility of breath-hold fast-recovery fast spin-echo t2 versus respiratory-triggered fast spin-echo T2 in clinical hepatic imaging. AJR Am J Roentgenol. 2005; 184:842–846. [PubMed: 15728606]
11. Lee SS, Byun JH, Hong HS, et al. Image quality and focal lesion detection on T2-weighted MR imaging of the liver: Comparison of two high-resolution free-breathing imaging techniques with two breath-hold imaging techniques. J Magn Reson Imaging. 2007; 26:323–330. [PubMed: 17610287]
12. Wile GE, Leyendecker JR. Magnetic resonance imaging of the liver: Sequence optimization and artifacts. Magn Reson Imaging Clin N Am. 2010; 18:525–547. [xi]. [PubMed: 21094454]
13. McFarland EG, Mayo-Smith WW, Saini S, et al. Hepatic hemangiomas and malignant tumors: Improved differentiation with heavily T2-weighted conventional spin-echo MR imaging. Radiology. 1994; 193:43–47. [PubMed: 8090920]
14. Ito K, Mitchell DG, Outwater EK, et al. Hepatic lesions: Discrimination of nonsolid, benign lesions from solid, malignant lesions with heavily T2-weighted fast spin-echo MR imaging. Radiology. 1997; 204:729–737. [PubMed: 9280251]
15. Bley TA, Wieben O, Francois CJ, et al. Fat and water magnetic resonance imaging. J Magn Reson Imaging. 2010; 31:4–18. [PubMed: 20027567]
16. Deshmane A, Gulani V, Griswold MA, et al. Parallel MR imaging. J Magn Reson Imaging. 2012; 36:55–72. [PubMed: 22696125]

17. Lauenstein TC, Sharma P, Hughes T, et al. Evaluation of optimized inversion-recovery fat-suppression techniques for T2-weighted abdominal MR imaging. J Magn Reson Imaging. 2008; 27:1448–1454. [PubMed: 18504735]
18. Scheffler K, Lehnhardt S. Principles and applications of balanced SSFP techniques. Eur Radiol. 2003; 13:2409–2418. [PubMed: 12928954]
19. Lee VS, Lavelle MT, Krinsky GA, et al. Volumetric MR imaging of the liver and applications. Magn Reson Imaging Clin N Am. 2001; 9:697–716. [v-vi]. [PubMed: 11694434]
20. Lee VS, Lavelle MT, Rofsky NM, et al. Hepatic MR imaging with a dynamic contrast-enhanced isotropic volumetric interpolated breath-hold examination: Feasibility, reproducibility, and technical quality. Radiology. 2000; 215:365–372.
21. Markl M, Leupold J. Gradient echo imaging. J Magn Reson Imaging. 2012; 35:1274–1289. [PubMed: 22588993]
22. Low RN, Francis IR, Herfkens RJ, et al. Fast multiplanar spoiled gradient-recalled imaging of the liver: Pulse sequence optimization and comparison with spin-echo MR imaging. AJR Am J Roentgenol. 1993; 160:501–509. [PubMed: 8381572]
23. Rofsky NM, Lee VS, Laub G, et al. Abdominal MR imaging with a volumetric interpolated breath-hold examination. Radiology. 1999; 212:876–884. [PubMed: 10478260]
24. Elsayes KM, Narra VR, Yin Y, et al. Focal hepatic lesions: Diagnostic value of enhancement pattern approach with contrast-enhanced 3D gradient-echo MR imaging. Radiographics. 2005; 25:1299–1320. [PubMed: 16160113]
25. Ream JM, Rosenkrantz AB. Advances in T1-weighted and T2-weighted imaging in the abdomen and pelvis. Radiol Clin North Am. 2015; 53:583–598. [PubMed: 25953291]
26. Rescinito G, Sirlin C, Cittadini G. Body MRI artefacts: From image degradation to diagnostic utility. Radiol Med (Torino). 2008; 114:18–31. [PubMed: 18836865]
27. Hernando D, Levin YS, Sirlin CB, et al. Quantification of liver iron with MRI: State of the art and remaining challenges. J Magn Reson Imaging. 2014; 40:1003–1021. [PubMed: 24585403]
28. Baron RL. Understanding and optimizing use of contrast material for CT of the liver. Am J Roentgenol. 1994; 163:323–331. [PubMed: 8037023]
29. American College of Radiology (ACR): Liver Imaging Reporting and Data System (LIRADS). 2014. Available at: https://nrdr.acr.org/lirads/
30. Gandhi SN, Brown MA, Wong JG, et al. MR contrast agents for liver imaging: What, when, how. Radiographics. 2006; 26:1621–1636. [PubMed: 17102040]
31. Sharma P, Kalb B, Kitajima HD, et al. Optimization of single injection liver arterial phase gadolinium enhanced MRI using bolus track real-time imaging. J Magn Reson Imaging. 2011; 33:110–118. [PubMed: 21182128]
32. Earls JP, Rofsky NM, DeCorato DR, et al. Hepatic arterial-phase dynamic gadolinium-enhanced MR imaging: Optimization with a test examination and a power injector. Radiology. 1997; 202:268–273. [PubMed: 8988222]
33. Foo TK, Saranathan M, Prince MR, et al. Automated detection of bolus arrival and initiation of data acquisition in fast, three-dimensional, gadolinium-enhanced MR angiography. Radiology. 1997; 203:275–280. [PubMed: 9122407]
34. Cogley JR, Miller FH. MR imaging of benign focal liver lesions. Radiol Clin North Am. 2014; 52:657–682. [PubMed: 24889166]
35. Jhaveri KS, Hosseini-Nik H. MRI of cholangiocarcinoma. J Magn Reson Imaging. 2015; 42:1165–1179. [PubMed: 25447417]
36. Brismar TB, Dahlstrom N, Edsborg N, et al. Liver vessel enhancement by Gd-BOPTA and Gd-EOB-DTPA: A comparison in healthy volunteers. Acta Radiol. 2009; 50:709–715. [PubMed: 19701821]
37. Bashir MR. Magnetic resonance contrast agents for liver imaging. Magn Reson Imaging Clin N Am. 2014; 22:283–293. [PubMed: 25086930]
38. Tamada T, Ito K, Sone T, et al. Dynamic contrast-enhanced magnetic resonance imaging of abdominal solid organ and major vessel: Comparison of enhancement effect between Gd-EOB-DTPA and Gd-DTPA. J Magn Reson Imaging. 2009; 29:636–640. [PubMed: 19243060]

39. Schalkx HJ, van Stralen M, Coenegrachts K, et al. Liver perfusion in dynamic contrast-enhanced magnetic resonance imaging (DCE-MRI): Comparison of enhancement in Gd-BT-DO3A and Gd-EOB-DTPA in normal liver parenchyma. Eur Radiol. 2014; 24:2146–2156. [PubMed: 24996795]
40. Frydrychowicz A, Nagle SK, D'Souza SL, et al. Optimized high-resolution contrast-enhanced hepatobiliary imaging at 3 Tesla: A cross-over comparison of gadobenate dimeglumine and gadoxetic acid. J Magn Reson Imaging. 2011; 34:585–594. [PubMed: 21751288]
41. Kühn J-P, Hegenscheid K, Siegmund W, et al. Normal dynamic MRI enhancement patterns of the upper abdominal organs: Gadoxetic acid compared with gadobutrol. Am J Roentgenol. 2009; 193:1318–1323. [PubMed: 19843748]
42. Zizka J, Klzo L, Ferda J, et al. Dynamic and delayed contrast enhancement in upper abdominal MRI studies: Comparison of gadoxetic acid and gadobutrol. Eur J Radiol. 2007; 62:186–191. [PubMed: 17367974]
43. Tirkes T, Mehta P, Aisen AM, et al. Comparison of dynamic phase enhancement of hepatocellular carcinoma using gadoxetate disodium vs gadobenate dimeglumine. J Comput Assist Tomogr. 2015; 39:479–482. [PubMed: 25783800]
44. Vogl TJ, Pegios W, McMahon C, et al. Gadobenate dimeglumine—A new contrast agent for MR imaging: Preliminary evaluation in healthy volunteers. Am J Roentgenol. 1992; 158:887–892. [PubMed: 1546612]
45. Kirchin MA, Pirovano GP, Spinazzi A. Gadobenate dimeglumine (Gd-BOPTA). An overview. Invest Radiol. 1998; 33:798–809. [PubMed: 9818314]
46. Food and Drug Administration. MultiHance. 2010. Available at: http://www.accessdata.fda.gov/drugsatfda_docs/label/2010/021357s009lbl.pdf
47. Food and Drug Administration. EOVIST (Gadoxetate Disodium). 2010. Available at: http://www.accessdata.fda.gov/drugsatfda_docs/label/2010/022090s004lbl.pdf
48. Bannas P, Motosugi U, Hernando D, et al. Combined gadoxetic acid and gadofosveset enhanced liver MRI: A feasibility and parameter optimization study. Magn Reson Med. 2016; 75:318–328. [PubMed: 25648403]
49. Haradome H, Grazioli L, Tsunoo M, et al. Can MR fluoroscopic triggering technique and slow rate injection provide appropriate arterial phase images with reducing artifacts on gadoxetic acid-DTPA (Gd-EOB-DTPA)-enhanced hepatic MR imaging? J Magn Reson Imaging. 2010; 32:334–340. [PubMed: 20677259]
50. Pietryga JA, Burke LM, Marin D, et al. Respiratory motion artifact affecting hepatic arterial phase imaging with gadoxetate disodium: Examination recovery with a multiple arterial phase acquisition. Radiology. 2014; 271:426–434. [PubMed: 24475864]
51. Guglielmo FF, Mitchell DG, Gupta S. Gadolinium contrast agent selection and optimal use for body MR imaging. Radiol Clin North Am. 2014; 52:637–656. [PubMed: 24889165]
52. Haradome H, Grazioli L, Almanea K, et al. Gadoxetic acid disodium-enhanced hepatocyte phase MRI: Can increasing the flip angle improve focal liver lesion detection? J Magn Reson Imaging. 2012; 35:132–139. [PubMed: 21960465]
53. Motosugi U, Ichikawa T, Onohara K, et al. Distinguishing hepatic metastasis from hemangioma using gadoxetic acid-enhanced magnetic resonance imaging. Invest Radiol. 2011; 46:359–365. [PubMed: 21427594]
54. Gupta RT, Marin D, Boll DT, et al. Hepatic hemangiomas: Difference in enhancement pattern on 3T MR imaging with gadobenate dimeglumine versus gadoxetate disodium. Eur J Radiol. 2012; 81:2457–2462. [PubMed: 22138122]
55. Grazioli L, Morana G, Kirchin MA, et al. Accurate differentiation of focal nodular hyperplasia from hepatic adenoma at gadobenate dimeglumine-enhanced MR imaging: Prospective study. Radiology. 2005; 236:166–177. [PubMed: 15955857]
56. Grazioli L, Bondioni MP, Faccioli N, et al. Solid focal liver lesions: Dynamic and late enhancement patterns with the dual phase contrast agent gadobenate dimeglumine. J Gastrointest Cancer. 2010; 41:221–232. [PubMed: 20405242]
57. Suh CH, Kim KW, Kim GY, et al. The diagnostic value of Gd-EOB-DTPA-MRI for the diagnosis of focal nodular hyperplasia: A systematic review and meta-analysis. Eur Radiol. 2015; 25:950–960. [PubMed: 25537979]

58. Shanbhogue A, Shah SN, Zaheer A, et al. Hepatocellular adenomas: Current update on genetics, taxonomy, and management. J Comput Assist Tomogr. 2011; 35:159–166. [PubMed: 21412084]

59. Grazioli L, Bondioni MP, Haradome H, et al. Hepatocellular adenoma and focal nodular hyperplasia: Value of gadoxetic acid-enhanced MR Imaging in differential diagnosis. Radiology. 2012; 262:520–529. [PubMed: 22282184]

60. Goodwin MD, Dobson JE, Sirlin CB, et al. Diagnostic challenges and pitfalls in MR imaging with hepatocyte-specific contrast agents. Radio-graphics. 2011; 31:1547–1568.

61. Zech CJ, Grazioli L, Jonas E, et al. Health-economic evaluation of three imaging strategies in patients with suspected colorectal liver metastases: Gd-EOB-DTPA-enhanced MRI vs. extracellular contrast media-enhanced MRI and 3-phase MDCT in Germany, Italy and Sweden. Eur Radiol. 2009; 19(suppl 3):S753–S763. [PubMed: 19484243]

62. Choi JY, Lee JM, Sirlin CB. CT and MR imaging diagnosis and staging of hepatocellular carcinoma: Part I. Development, growth, and spread: Key pathologic and imaging aspects. Radiology. 2014; 272:635–654. [PubMed: 25153274]

63. Sano K, Ichikawa T, Motosugi U, et al. Imaging study of early hepatocellular carcinoma: Usefulness of gadoxetic acid-enhanced MR imaging. Radiology. 2011; 261:834–844. [PubMed: 21998047]

64. Choi JY, Lee JM, Sirlin CB. CT and MR imaging diagnosis and staging of hepatocellular carcinoma: Part II. Extracellular agents, hepatobiliary agents, and ancillary imaging features. Radiology. 2014; 273:30–50. [PubMed: 25247563]

65. Tsuboyama T, Onishi H, Kim T, et al. Hepatocellular carcinoma: Hepatocyte-selective enhancement at gadoxetic acid-enhanced MR imaging—Correlation with expression of sinusoidal and canalicular transporters and bile accumulation. Radiology. 2010; 255:824–833. [PubMed: 20501720]

66. Vilgrain V, Van Beers BE, Pastor CM. Insights into the diagnosis of hepatocellular carcinomas with hepatobiliary MRI. J Hepatol. 2015

67. Kitao A, Matsui O, Yoneda N, et al. Hepatocellular carcinoma with beta-catenin mutation: Imaging and pathologic characteristics. Radiology. 2015; 275:708–717. [PubMed: 25668519]

68. Golfieri R, Grazioli L, Orlando E, et al. Which is the best MRI marker of malignancy for atypical cirrhotic nodules: Hypointensity in hepatobiliary phase alone or combined with other features? Classification after Gd-EOB-DTPA administration. J Magn Reson Imaging. 2012; 36:648–657. [PubMed: 22592930]

69. Mannelli L, Bhargava P, Osman SF, et al. Diffusion-weighted imaging of the liver: A comprehensive review. Curr Probl Diagn Radiol. 2013; 42:77–83. [PubMed: 23683849]

70. Galea N, Cantisani V, Taouli B. Liver lesion detection and characterization: Role of diffusion-weighted imaging. J Magn Reson Imaging. 2013; 37:1260–1276. [PubMed: 23712841]

71. Wu L-M, Hu J, Gu H-Y, et al. Can diffusion-weighted magnetic resonance imaging (DW-MRI) alone be used as a reliable sequence for the preoperative detection and characterisation of hepatic metastases? A meta-analysis. Eur J Cancer. 2013; 49:572–584. [PubMed: 23000072]

72. Mannelli L, Nougaret S, Vargas HA, et al. Advances in diffusion-weighted imaging. Radiol Clin North Am. 2015; 53:569–581. [PubMed: 25953290]

73. Lewis S, Dyvorne H, Cui Y, et al. Diffusion-weighted imaging of the liver: Techniques and applications. Magn Reson Imaging Clin N Am. 2014; 22:373–395. [PubMed: 25086935]

74. Costello JR, Kalb B, Chundru S, et al. MR imaging of benign and malignant biliary conditions. Magn Reson Imaging Clin N Am. 2014; 22:467–488. [PubMed: 25086940]

75. Sandrasegaran K, Lin C, Akisik FM, et al. State-of-the-art pancreatic MRI. Am J Roentgenol. 2010; 195:42–53. [PubMed: 20566796]

76. Manfredi, R.; Bellotti, M.; Brandalise, A., et al. Magnetic resonance chol-angiopancreatography: Technical considerations. In: Manfredi, R.; Mucelli Pozzi, R., editors. Magnetic Resonance Cholangiopancreatography Biliary and Pancreatic Ducts. Springer; 2013. http://dx.doi.org/10.1016/j.rcl.2015.01.002

77. Kim SJ, Lee JM, Lee ES, et al. Preoperative staging of gallbladder carcinoma using biliary MR imaging. J Magn Reson Imaging. 2015; 41:314–321. [PubMed: 24470425]

78. Heyn C, Sue-Chue-Lam D, Jhaveri K, et al. MRI of the pancreas: Problem solving tool. J Magn Reson Imaging. 2012; 36:1037–1051. [PubMed: 23090915]
79. Palmucci S, Mauro LA, Coppolino M, et al. Evaluation of the biliary and pancreatic system with 2D SSFSE, breathhold 3D FRFSE and respiratory-triggered 3D FRFSE sequences. Radiol Med. 2010; 115:467–482. [PubMed: 20077045]
80. Wells SA. Quantification of hepatic fat and iron with magnetic resonance imaging. Magn Reson Imaging Clin N Am. 2014; 22:397–416. [PubMed: 25086936]
81. Reeder SB, Sirlin C. Quantification of liver fat with magnetic resonance imaging. Magn Reson Imaging Clin N Am. 2010; 18:337–357. [PubMed: 21094444]
82. Reeder SB, Cruite I, Hamilton G, et al. Quantitative assessment of liver fat with magnetic resonance imaging and spectroscopy. J Magn Reson Imaging. 2011; 34:1629–1634. spcone.
83. Bannas P, Kramer H, Hernando D, et al. Quantitative magnetic resonance imaging of hepatic steatosis: Validation in ex vivo human livers. Hepatology. 2015; 62:1444–1455. [PubMed: 26224591]
84. Serai SD, Fleck RJ, Quinn CT, et al. Retrospective comparison of gradient recalled echo R2* and spin-echo R2 magnetic resonance analysis methods for estimating liver iron content in children and adolescents. Pediatr Radiol. 2015; 45:1629–1634. [PubMed: 26008870]
85. Wood JC, Enriquez C, Ghugre N, et al. MRI R2 and R2(*) mapping accurately estimates hepatic iron concentration in transfusion-dependent thalassemia and sickle cell disease patients. Blood. 2005; 106:1460–1465. [PubMed: 15860670]
86. Yokoo T, Browning JD. Fat and iron quantification in the liver: Past, present, and future. Top Magn Reson Imaging. 2014; 23:73–94. [PubMed: 24690618]
87. Krafft AJ, Loeffler RB, Song R, et al. Does fat suppression via chemically selective saturation affect R2*-MRI for transfusional iron overload assessment? A clinical evaluation at 1.5 T and 3 T. Magn Reson Med. 2015
88. Ellis EL, Mann DA. Clinical evidence for the regression of liver fibrosis. J Hepatol. 2012; 56:1171–1180. [PubMed: 22245903]
89. Bedossa P, Poynard T. An algorithm for the grading of activity in chronic hepatitis C. Hepatology. 1996; 24:289–293. [PubMed: 8690394]
90. Ishak K, Baptista A, Bianchi L, et al. Histological grading and staging of chronic hepatitis. J Hepatol. 1995; 22:696–699. [PubMed: 7560864]
91. Venkatesh SK, Yin M, Ehman RL. Magnetic resonance elastography of liver: Technique, analysis, and clinical applications. J Magn Reson Imaging. 2013; 37:544–555. [PubMed: 23423795]
92. Godfrey EM, Mannelli L, Griffin N, et al. Magnetic resonance elastography in the diagnosis of hepatic fibrosis. Semin Ultrasound CT MR. 2013; 34:81–88. [PubMed: 23395320]
93. Singh S, Venkatesh SK, Wang Z, et al. Diagnostic performance of magnetic resonance elastography in staging liver fibrosis: A systematic review and meta-analysis of individual participant data. Clin Gastroenterol Hepatol. 2015; 13:440–451. [e446]. [PubMed: 25305349]
94. Hennedige TP, Hallinan JT, Leung FP, et al. Comparison of magnetic resonance elastography and diffusion-weighted imaging for differentiating benign and malignant liver lesions. Eur Radiol. 2016; 26:398–406. [PubMed: 26032879]
95. Ahn SJ, Kim MJ, Hong HS, et al. Distinguishing hemangiomas from malignant solid hepatic lesions: A comparison of heavily T2-weighted images obtained before and after administration of gadoxetic acid. J Magn Reson Imaging. 2011; 34:310–317. [PubMed: 21598345]
96. Kim YK, Kwak HS, Kim CS, et al. Detection and characterization of focal hepatic tumors: A comparison of T2-weighted MR images before and after the administration of gadoxectic acid. J Magn Reson Imaging. 2009; 30:437–443. [PubMed: 19629973]
97. Choi SA, Lee SS, Jung IH, et al. The effect of gadoxetic acid enhancement on lesion detection and characterisation using T(2) weighted imaging and diffusion weighted imaging of the liver. Br J Radiol. 2012; 85:29–36. [PubMed: 21123305]
98. Muhi A, Ichikawa T, Motosugi U, et al. Diffusion- and T(2)-weighted MR imaging of the liver: Effect of intravenous administration of gadoxetic acid disodium. Magn Reson Med Sci. 2012; 11:185–191. [PubMed: 23037563]

99. Saito K, Araki Y, Park J, et al. Effect of Gd-EOB-DTPA on T2-weighted and diffusion-weighted images for the diagnosis of hepatocellular carcinoma. J Magn Reson Imaging. 2010; 32:229–234. [PubMed: 20578029]

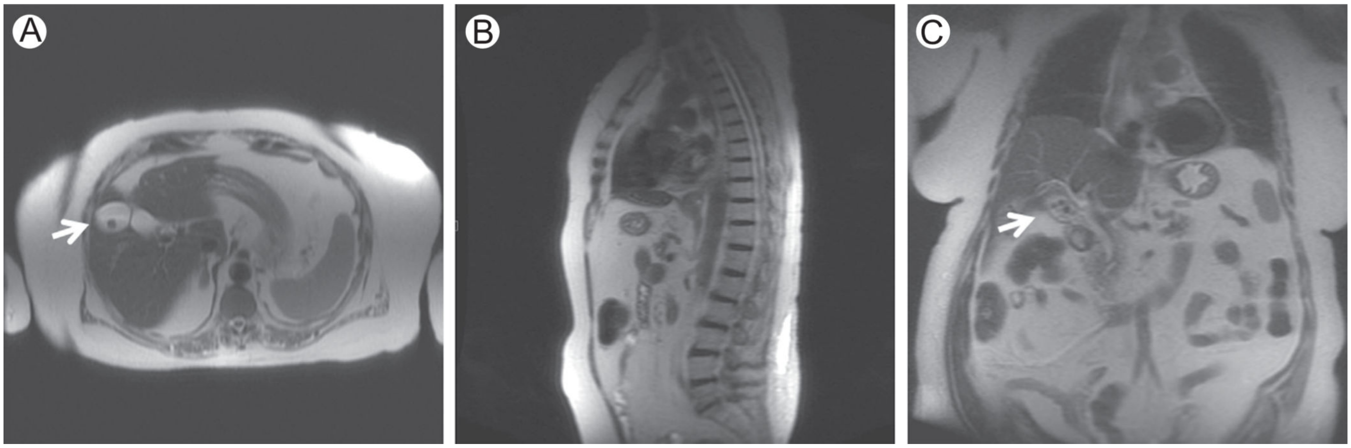

Figure 1.

Localizer. SSFSE T2-weighted (TE = 80 milliseconds) on axial (A), sagittal (B), and coronal (C) planes. In our institution, the localizer is acquired with T2-weighted SSFSE sequence, with a low number of thick slices on the axial, sagittal, and coronal planes (7 slices for each plane; slice thickness = 8 mm). Images A and C show the collateral finding of gallstones (white arrows) in a 74-year-old woman with melanoma.

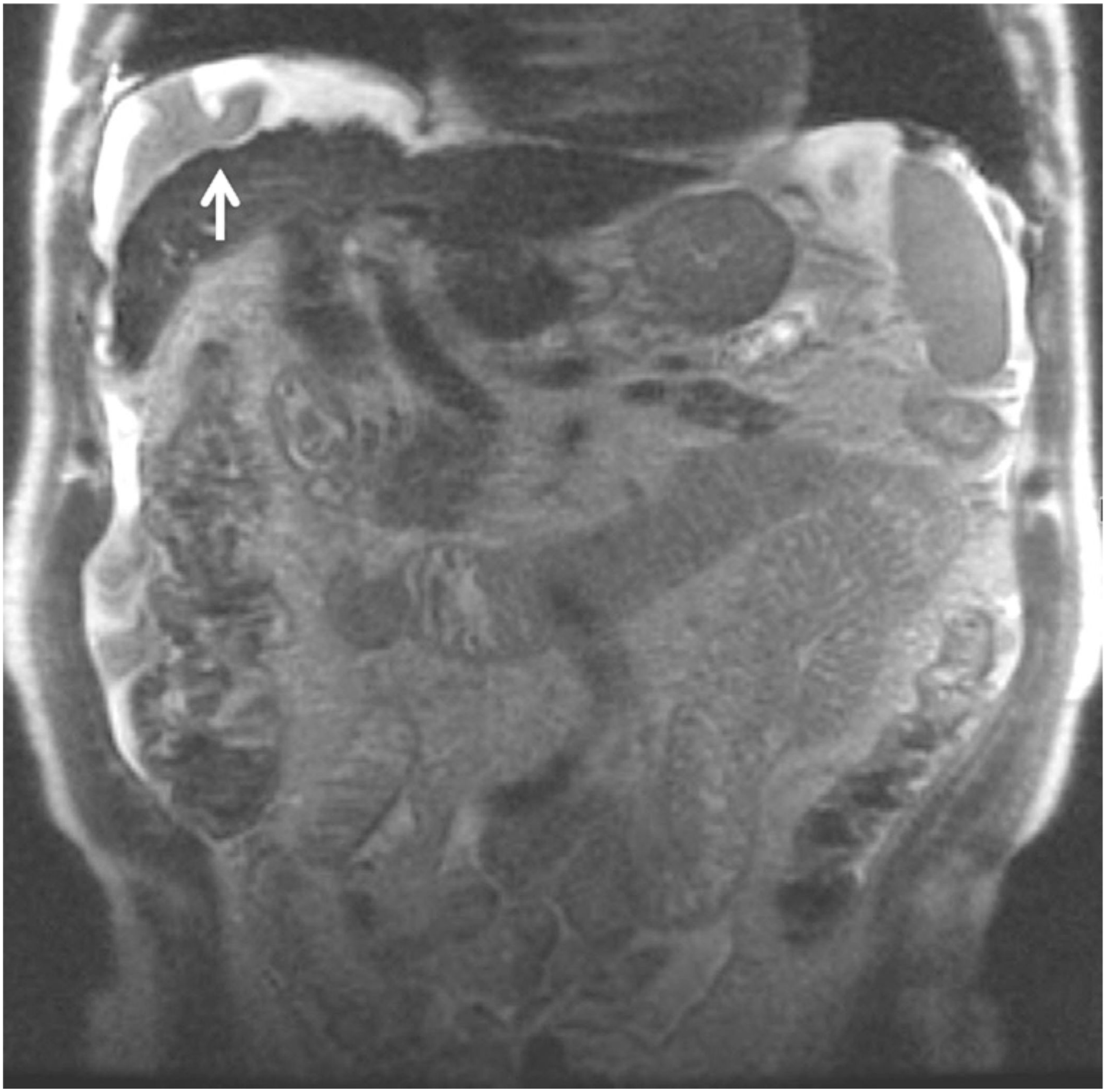

Figure 2.

SSFSE T2-weighted, coronal (TE = 99 milliseconds, slice thickness = 4 mm). Coronal T2-weighted images are useful to obtain an overview of the upper abdomen, in particular, to evaluate the extension of fluid collections. In this 84-year-old man with liver cirrhosis, a perihepatic collection is present, with artifacts due to fluid movements (white arrow).

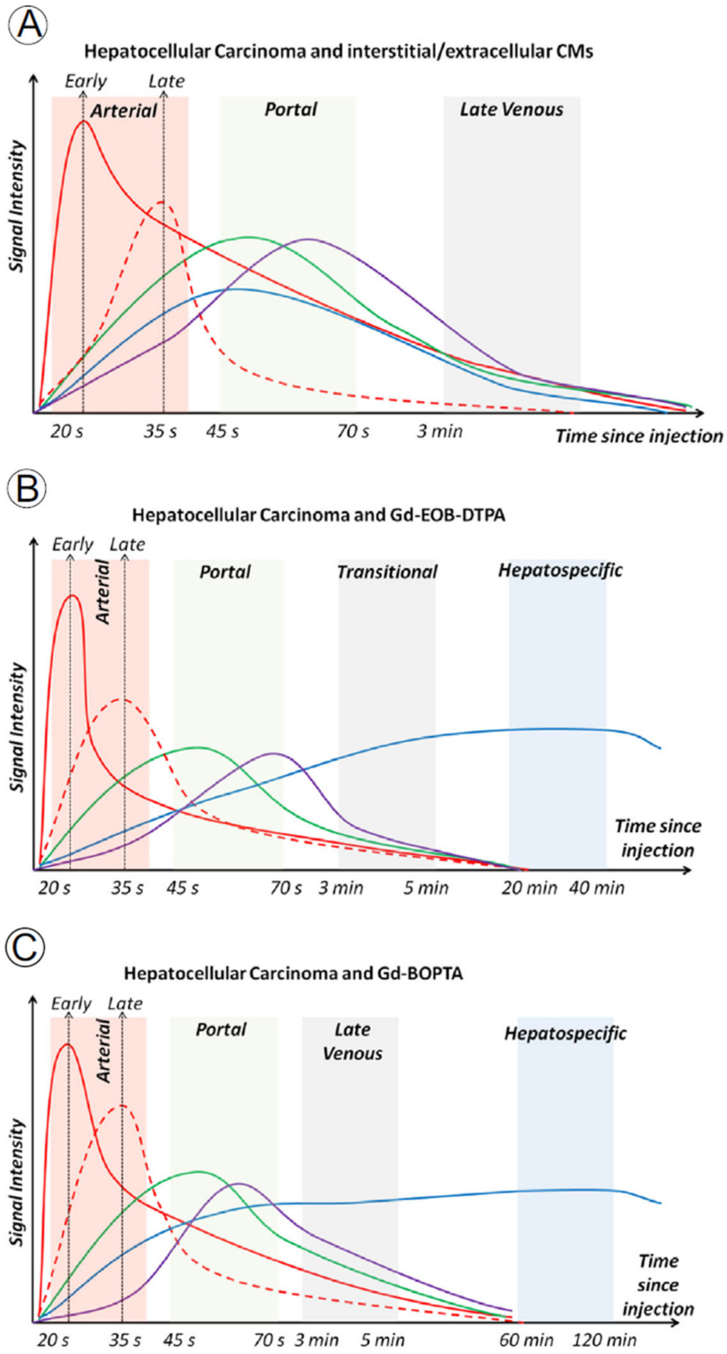

Figure 3.

(A–C) Enhancement curves with signal intensity plotted against time. Red line: abdominal aorta. Red dashed line: hepatocellular carcinoma (HCC). Green line: portal vein. Purple line: hepatic vein. Blue line: hepatic parenchyma. Red shadow: arterial phase. Green shadow: portal phase. Gray shadow: delayed-transitional phase. Blue shadow: hepatospecific phase. (A) Enhancement curves with extracellular or interstitial CM. Hepatocellular carcinoma has late arterial enhancement. During portal and venous phase, the HCC washout is evident (HCC signal is lower than liver parenchyma). After the late venous phase, vascular and parenchymal signals decrease because of renal excretion. (B) Enhancement curves with Gd-EOB-DTPA. The enhancement peak of HCC tends to be lower than that of other CM. The rapid hepatocellular uptake results in increasing liver signal until a plateau at 20 minutes, whereas vascular signals tend to decrease rapidly. (C) Enhancement curves with Gd-BOPTA. The hepatospecific phase is after 60 minutes, and vascular signals decrease earlier than in (B). (Color version of figure is available online.)

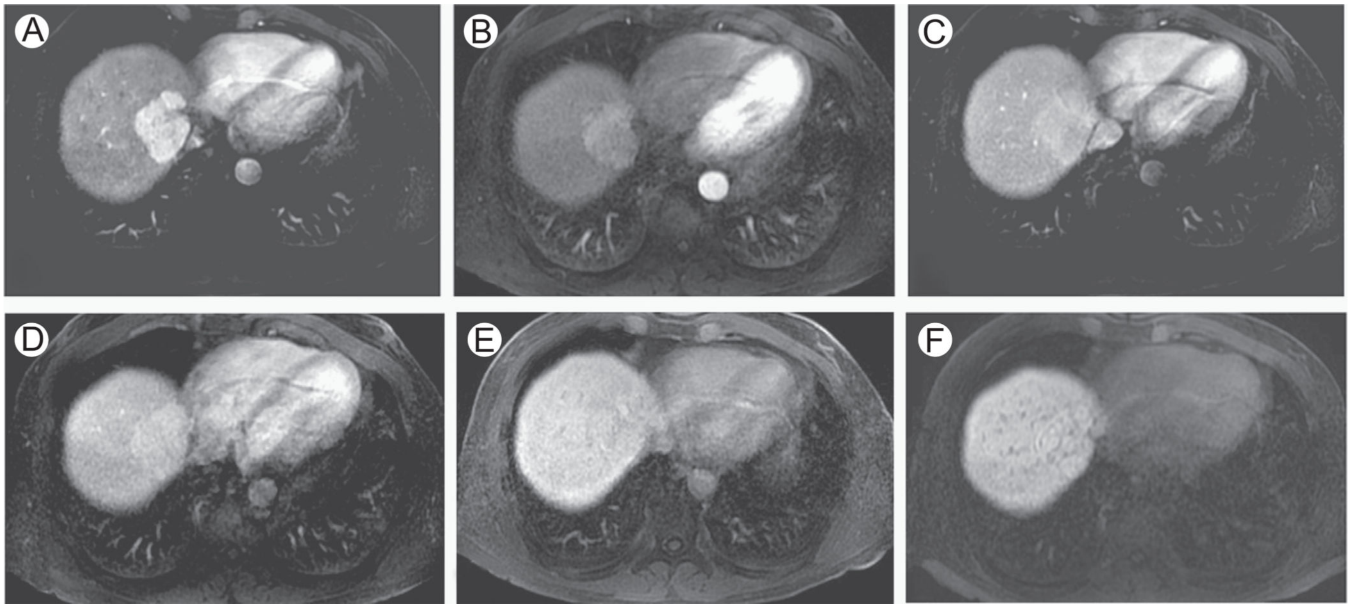

Figure 4.

Focal nodular hyperplasia, evaluation with Gd-BOPTA and Gd-EOB-DTPA. A 50-year-old man with focal nodular hyperplasia (FNH). Axial 3D SPGR fat suppressed (LAVA, slice thickness or overlay: 4 mm/2 mm). Images acquired in the arterial phase (A and B), portal venous phase (C and D), and hepatobiliary phase (E and F), after the administration of Gd-BOPTA (A, C, and E) and Gd-EOB-DTPA (B, D, and F) in 2 different examinations. Typically, FNH are hyperenhancing in the arterial phase (A and B) with active uptake of CM in the hepatospecific phase (E—90 minutes since injection of Gd-BOPTA; F—20 minutes since injection of Gd-EOB-DTPA). (F) The rapid hepatocellular uptake of Gd-EOB-DTPA, together with renal elimination, results in hypointensity of intrahepatic vascular structures, visible as hypointense spot scattered in hepatic parenchyma. LAVA, liver acquisition volume acceleration.

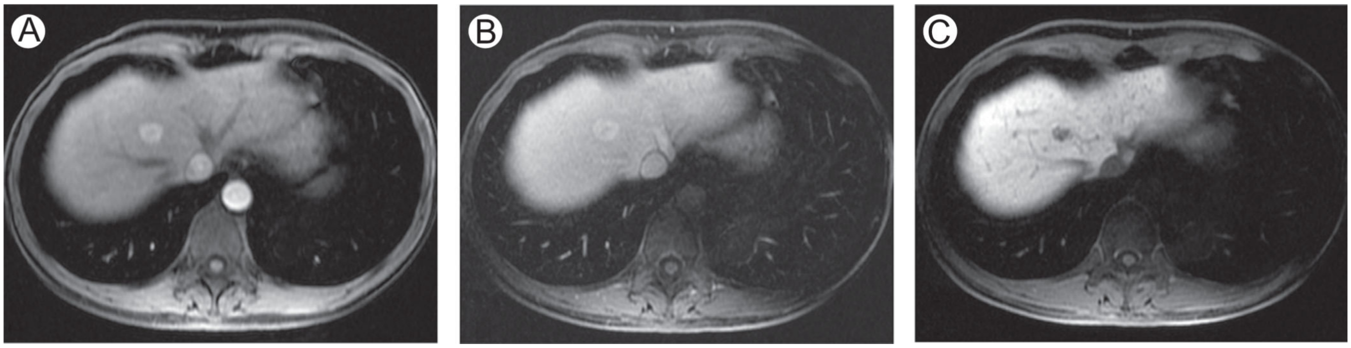

Figure 5.

Hepatocellular adenoma. (A–C) Axial 3D SPGR fat suppressed (LAVA, slice thickness or overlay: 5 mm/2.5 mm), acquired after the administration of Gd-EOB-DTPA in the arterial (A), late venous (B), and hepatobiliary phase (C). Images show a hepatocellular adenoma (HA) in a 49-year-old woman with history of oral contraceptives. In contrast to FNH (Figure 4), HA does not have active uptake of CM in the hepatospecific phase (C—At 20 minutes since injection of Gd-EOB-DTPA). As in Figure 4F, (C) the rapid clearance of Gd-EOB-DTPA from vascular compartment results in hypointensity of intrahepatic vascular structures. LAVA, liver acquisition volume acceleration.

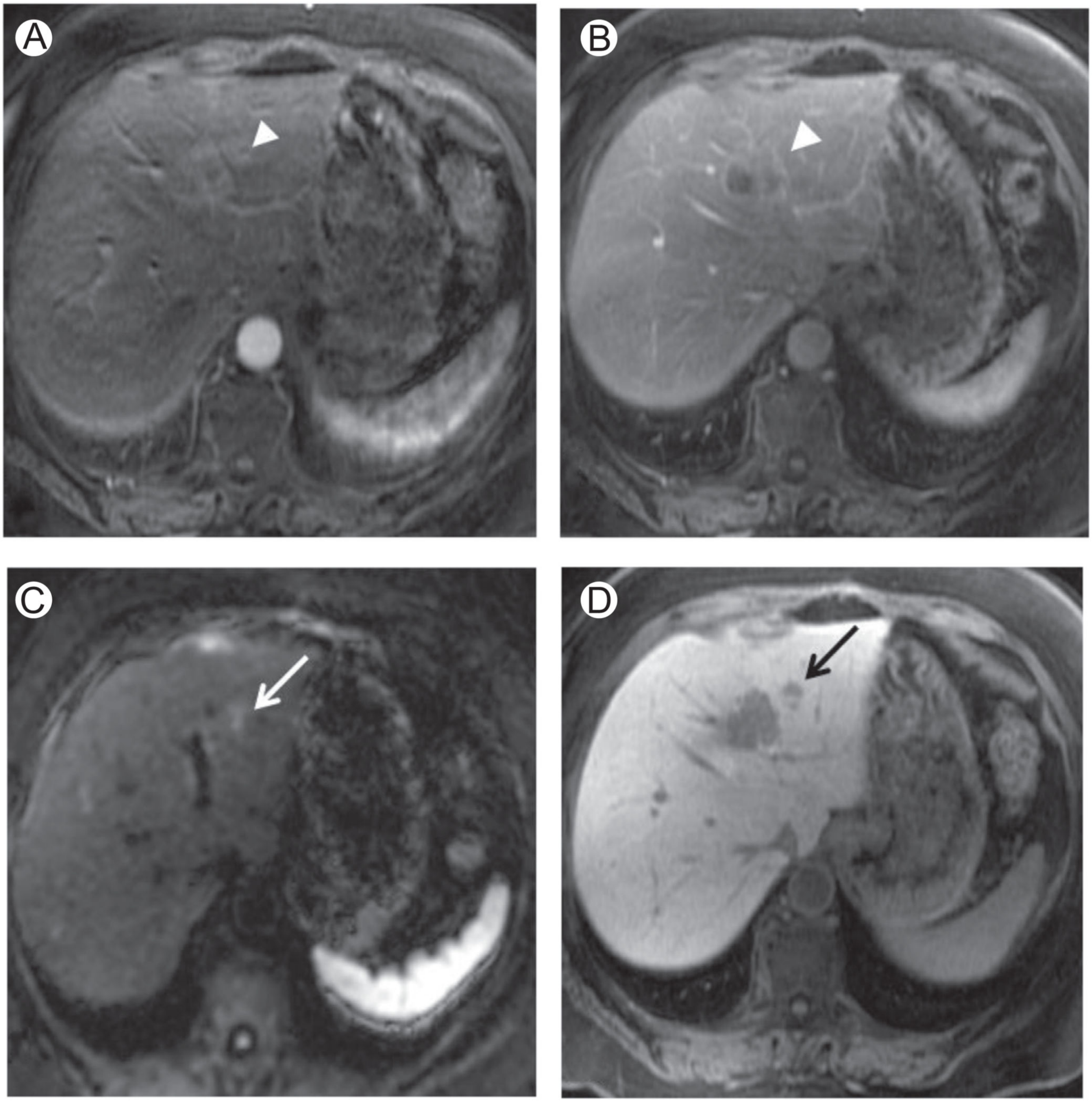

Figure 6.

Liver metastases. A 54-year-old woman with colorectal liver metastases. (A, B, and D) Axial 3D SPGR fat suppressed (LAVA, slice thickness or overlay: 5 mm/2.5 mm), respectively, in the arterial (A), portal venous (B), and hepatospecific (D) phase after administration of Gd-EOB-DTPA. (C) DWI, $b = 500$ s/mm^2 (slice thickness or spacing: 7 mm/8 mm). In the arterial phase (A), the white arrowhead shows a colorectal liver metastasis in segment II-IVa as a slightly hypervascular area, hypointense in the portal venous phase (B—white arrowhead). The DWI at high *b* value shows an area of restricted diffusion near the lesion depicted in A and B, corresponding to a second smaller metastasis as confirmed by the black arrow in the hepatobiliary phase D. LAVA, liver acquisition volume acceleration.

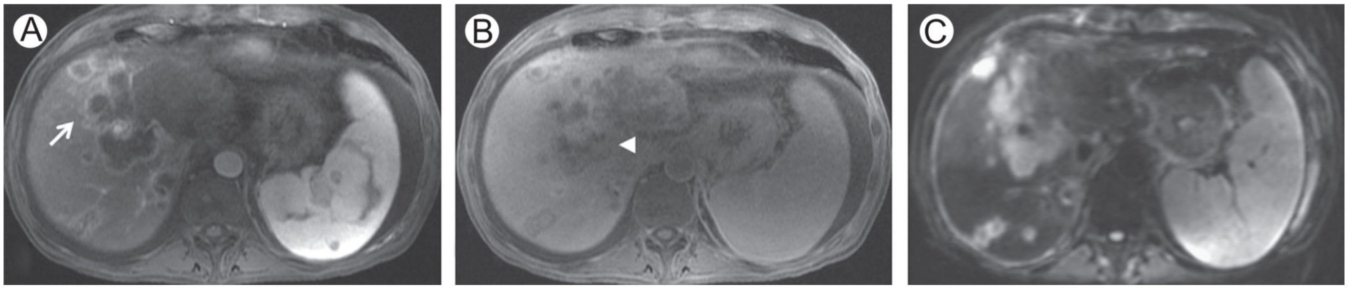

Figure 7.

Cholangiocellular carcinoma in a 54-year-old man. (A and B) Axial 3D SPGR fat suppressed (LAVA, slice thickness or overlay: 5 mm/2.5 mm), respectively, in the arterial (A) and hepatospecific (B) phases after administration of Gd-EOB-DTPA. (C): DWI, $b = 500$ s/mm^2 (slice thickness or spacing: 7 mm/8 mm). Images show an extensive cholangiocellular carcinoma with intrahepatic metastases. (A) Typical peripheral enhancement in the arterial phase (white arrow) with mild retention of Gd-EOB-DTPA in the desmoplastic component in the hepatospecific phase (B—white arrowhead). DWI at $b = 500$ shows inhomogeneous signal of the tumor and intrahepatic metastases (C). LAVA, liver acquisition volume acceleration.

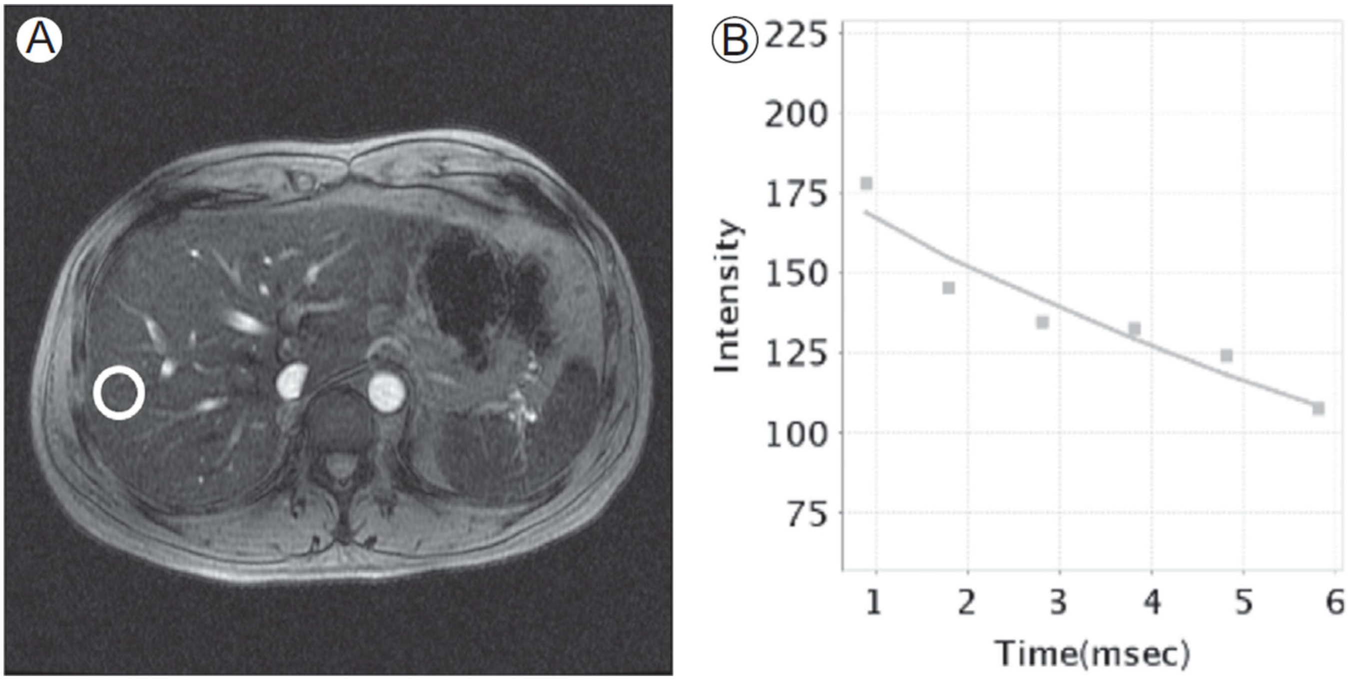

Figure 8.

Iron quantification with concomitant liver steatosis. (A) Axial T2*-weighted image from a multiecho T2* GRE (TR = 43 milliseconds, TE = 13 milliseconds). A free-hand ROI is placed in the liver parenchyma, avoiding visible vessels. (B) In this subject, a sinusoidal signal decay with poor fitting of measurements with exponential curve is characteristic of concomitant presence of liver steatosis and iron overload. Liver steatosis reduces accuracy in iron estimation. ROI, region of interest.

Table 1

Routine Liver Protocol With Injection of Extracellular or Interstitial CM

Description	T2w Coronal	T1w In/Out	T2w FatSat	DWI *b*= 0, 50, 500	T1w pre-CM	Bolus Tracking		
						Arterial	**Portal Venous**	**Delayed**
Sequence	SSFSE	3D SPGR (2D SPGR)	FRFSE	EPI	3D SPGR	3D SPGR		
Plane	Coronal	axial	Axial	Axial	Axial	Axial		
Slice thickness (mm)	5 (4)	4–5 (7)	7	7	4–5	4–5		
Gap (mm)	0	−2 to −2.5 (1)	1	1	−2 to −2.5	−2 to −2.5		
Fat Suppression	–	(Dixon)	Spectr	(Spectr)	Dixon/IR	Dixon/IR		
TE1/TE2 (ms) (out/in)	100	1.1/2.1 (2.2/4.4)	102	Min (<90)	1.4–2	1.4–2		
TR	–	4.5 (210)	2500	6000 (4000)	4.5	4.5		
Flip angle (°)	90	12 (90)	90	90	12	12		
ETL	–	–	13	–	–	–		
NEX	0.5	<1 (1)	2 (3)	1 (12)	<1	<1		
Phase enc. steps	224 (256)	192 (128)	224 (192)	128	192	192		
Frequency steps	320 (256)	320 (256)	320	128	300	300		
Breath	BH	BH	Trig.	BH/Trig.	BH	BH		
Notes						Peak + 5 s	Peak+60 s	Peak+180 s

Example of data for 3 T magnets; numbers in brackets are for 1.5 T. Postcontrast study is performed at the end of the protocol. Postcontrast study is performed with bolus tracking technique, with time since aortic peak reported in the last line. BH, breath-hold; Dixon, Dixon technique; enc., encoding; ETL, echo train length; FatSat, fat saturated; FSE, fast spin echo; IR, inversion recovery; In/out, in-phase and out-of-phase; NEX, number of excitations; Peak, aortic peak detected with bolus tracking; pre-CM, before contrast administration; Spectr., chemically selective fat suppression; SSFSE, half Fourier single-shot FSE; Trig, respiratory triggering; w, weighted.

Table 2

Liver Protocol, Injection of Gd-EOB-DTPA

Description	**T1w In/Out**	**T1w Pre-C**	**M Bolus Tracking, Injection Rate 1 mL/s**				
			Arterial Portal Venous Transitional	**T2w Coronal**	**T2w FatSat**	**DWI *b*= 0, 50, 500**	**Hepato-Specific**
Sequence	3D SPGR (2D SPGR)		3D SPGR	SSFSE	FRFSE	EPI	3D SPGR
Plane	axial	Axial	Axial	Coronal	Axial	Axial	Axial
Slice thickness (mm)	4–5 (7)	4–5	4–5	5 (4)	7	7	4–5
Gap (mm)	−2 to −2.5 (1)	−2 to −2.5	−2 to −2.5	0	1	1	−2 to −2.5
Fat suppression			Dixon/IR	–	Spectr.	(Spectr.)	Dixon/IR
TE1/TE2 (ms) (out/in)	1.1/2.1 (2.2/4.4)	1.4–2	1.4–2	100	102	Min (o90)	1.4–2
TR	4.5 (210)	4.5	4.5	–	2500	6000 (4000)	4.5
Flip angle	12 (90)	12	12	90	90	90	12
ETL	–	–	–	–	13	–	–
NEX	<1 (1)	<1	<1	0.5	2 (3)	1 (12)	o1
Phase enc. steps	192(128)	192	192	224(256)	224(192)	128	192
Frequency steps	320 (256)	300	300	320 (256)	320	128	300
Breath	BH	BH	BH	BH	Trig.	BH/Trig.	BH
Notes			Peak+5s dual arterial	Peak+60s	Peak+180s		Peak+20 min

Example of data for 3 T magnets; numbers in brackets are for 1.5 T. T2-weighted sequences are acquired after the administration of Gd-EOB-DTPA. Gd-EOB-DTPA is injected at 1 mL/s. BH, breath-hold; Dixon, Dixon technique; enc., encoding; ETL, echo train length; FatSat, fat saturated; FSE, fast spin echo; IR, inversion recovery; In/out, in-phase and out-of-phase; NEX, number of excitations; Peak, aortic peak detected with bolus tracking; pre-CM, before contrast administration; Spectr., chemically selective fat suppression; SSFSE, half Fourier single-shot FSE; Trig, respiratory triggering; w, weighted.

Table 3

Magnetic Resonance Cholangiopancreatography (MRCP), Injection of Extracellular or Interstitial CM

Description	**T2w Coronal**	**T1w In/Out**	**T2w Axial**	**T2w FatSat**	**DWI *b*= 0, 50, 500**	**T1w Pre-CM**	**Bolus Tracking**		
							Arterial Portal Venous	**Delayed 3D MRCP**	**2D MRCP**
Sequence	SSFSE	3D SPGR (2D SPGR)	SSFSE	FRFSE	EPI	3D SPGR	3D SPGR	3D FRFSE	SSFSE
Plane	Coronal	Axial	Axial	Axial	Axial	Axial	Axial	Coronal	Coronal
Slice Thickness (mm)	4	4–5 (7)	4	7	7	4–5	4–5	1.4	40
Gap (mm)	0	−2 to −2.5 (1)	0	1	1	−2 to −2.5	−2 to −2.5	−0.7	(9 slices radial)
Fat suppression	–	(Dixon)	–	Spectr.	(Spectr.)	Dixon/IR	Dixon/IR	–	–
TE1/TE2 (ms) (out/in	100	1.1/2.1 (2.2/4.4)	100	102	Min (<90)	1.4–2	1.4–2	~400	~ 1100
TR (mm)	–	4.5 (210)	–	2500	4000 (2000)	4.5	4.5	−2300	–
Flip angle	90	12 (90)	90	90	90	12	12	90	90
ETL	–	–	–	13	–	–	–	23	–
NEX	0.5	<1 (1)	0.5	1 (3)	1 (12)	<1	<1	1	
Phase enc. steps	224 (256)	192 (160)	224 (256)	224 (192)	128	192	192	320 (256)	512 (320)
Frequency steps	320 (256)	320 (256)	320 (256)	320	128	300	300	320 (256)	256
Breath	BH	BH	BH	BH	BH/Trig.	BH	BH	Trig.	BH
Notes							Peak + 5 s	Peak + 60 s	Peak + 180 s

Example of data for 3 T magnets; numbers in brackets are for 1.5 T. T2-weighted images are acquired before injection of CM, whereas MRCP is performed after the administration of CM. BH, breath-hold; Dixon, Dixon technique; enc., encoding; ETL, echo train length; FatSat, fat saturated; FSE, fast spin echo; IR, inversion recovery; In/out, in-phase and out-of-phase; NEX, number of excitations; Peak, aortic peak detected with bolus tracking; pre-CM, before contrast administration; Spectr., chemically selective fat suppression; SSFSE, half Fourier single-shot FSE; Trig, respiratory triggering; w, weighted.

Table 4

Liver Iron Quantification

Description	T2w Coronal	T1w In/ Out	T2w FatSat	DWI *b*= 0, 50, 500	T1w Axial	T2*MAP In-Phase	T2*MAP Short ET	T2*MAP Long ET
Sequence	SSFSE	2D SPGR	FRFSE	EPI	3D SPGR	2D GRE	2D GRE	2D GRE
Plane	Coronal	Axial	Axial	Axial	Axial	Axial	Axial	Axial
Slice thickness (mm)	5	7	7	7	5	10 (3 slices)	10 (3 slices)	10 (3 slices)
Gap (mm)	0	1	1	1	−2.5	2	2	2
Fat suppression	–	–	Spectr.	(Spectr.)	IR	–	–	–
TE1/TE2 (ms) (out/in)	100	2.2/4.4	102	Min (<90)	?	1.9; 4.7; 7.5; 10.2; 13; 15.8; 18.5; 21.3	0.9; 1.8; 2.8; 3.8; 4.8; 5.8	0.9; 2.0; 3.1; 4.2; 5.3; 6.4; 7.6; 8.7; 9.8; 10.9; 12; 13.1
TR (ms)	–	210	2500	4000 (2000)	?	−40	35.5	35.5
Flip angle	90	90	90	90	12	25	12	12
ETL	–	–	15	–	–	–	–	–
NEX	0.5	1	1	1 (12)	<1	1	1	1
Phase enc. steps	320	256	256	128	256	384	128	104
Frequency steps	192	128	160	128	192	192	64	104
Breath	BH	BH	BH	BH/Trig.	BH	BH	BH	BH
Notes						8 echoes	6 echoes	12 echoes

After basic sequences for evaluation of liver parenchyma, 3 multiecho T2*-weighted sequences are acquired to obtain good accuracy in estimation. In the first T2*-weighted series, ETs are set approximately within water and fat phase coherence, whereas in short ET the first echo time is <1 ms to investigate higher iron concentrations. The long ET series is designed to investigate lower iron concentrations. BH, breath-hold; Dixon, Dixon technique; enc., encoding; ETL, echo train length; FSE, fast spin echo; In/out, in-phase and out-of-phase; IR, inversion recovery; NEX, number of excitations; Spectr., chemically selective fat suppression; SSFSE, half Fourier single-shot FSE. Trig., respiratory triggering; w, weighted.